Journal of Materials Chemistry A

Accepted Manuscript

ROYAL SOCIETY OF CHEMISTRY

www.rsc.org/materialsA

Self-assembled graphene aerogel and nanodiamond hybrid as high performance catalyst in oxidative propane dehydrogenation

Laura Roldan, Ana M. Benito, Enrique García-Bordejé*,

Instituto de Carboquímica (ICB-CSIC), Miguel Luesma Castán 4, E-50018 Zaragoza, Spain, jegarcia@icb.csic.es

Keywords

Graphene aerogel, nanodiamond hybrid, propane dehydrogenation

Abstract

Graphene aerogel and graphene aerogel-nanodiamond hybrids have been fabricated by a mild reduction/self-assembly hydrothermal method using graphene oxide dispersion as precursor. The aerogels have been used as metal-free catalyst for oxidative dehydrogenation of propane. Reduced graphene oxide (RGO) aerogel without nanodiamond outperformed carbon nanotubes in terms of propene productivity and selectivity, which is correlated to a higher content of accessible carbonyl-quinone groups and more defective structure of reduced graphene oxide. Graphene aerogel loaded with low amounts of nanodiamonds (2 wt%) by one-pot strategy provided 18% higher activity than RGO aerogel, ascribed to the increase of the sp^3/sp^2 ratio. For nanodiamond contents higher than 2 wt%, the productivity and selectivity drops, which can be explained by a dramatic decrease of carbonyl-quinone groups, an increased content of unselective oxygen species and clustering of nanodiamonds for the highest

* Corresponding author: Tel.:+ 34 976733977; fax.: +34 976733318 *E-mail address:* jegarcia@icb.csic.es

loadings. The hybrid aerogels are freestanding, robust and highly porous monoliths, thereby a suitable platform to be used as catalyst or adsorbent in flow systems.

Introduction

Graphene oxide (GO) can be regarded as a 2D network consisting of variable concentrations of sp^2 and sp^3 carbon. GO is thought to contain epoxy and hydroxyl groups on the basal plane with various other types of oxygen groups at the graphene edges.[1,2] Additionally, high-resolution ^{13}C NMR spectroscopy has revealed the presence of lactol, ester carbonyl, and ketone functional groups at the edges or defects of graphene oxide.[3] The proposed structure of graphene oxide[4] consist of five- and six-membered lactol rings decorating the edges and esters of tertiary alcohols on the surface. Although most the hydroxyl and epoxy functional groups can be removed after the reduction of graphene oxide, the holes, Stone–Wales and other defects are usually observed within the basal plane. Besides, highly stable carbonyl and ether groups also remain at the edges/defects.[5] In addition, graphene oxide can contain some trace amounts of other heteroatom-containing functionalities, such as sulfate groups, introduced during the preparation of graphite oxide by the Hummers method.[6]

Theoretical studies have predicted a high activity of GO in the oxidative dehydrogenation (ODH) of propane due to the oxygen groups present on its surface.[7] This is an important reaction for petrochemical industry. Nowadays, the olefins are essentially obtained by steam cracking of naphtha fractions or fluid catalytic cracking (FCC). However, the established steam cracking and FCC technologies are unable to provide sufficient olefins according to the market demand and thus, new catalytic processes are needed to perform the direct transformation of light alkanes into olefins with low environmental impact and high efficiency.[8,9]

In recent years, carbon materials have drew significant attention as metal-free catalyst for oxidative dehydrogenation of alkanes. Many types of carbon based structures have been claimed to be active and selective, including activated carbons,[10,11] onion-like carbons,[12-14] carbon nanofibers,[15-21] activated fibers,[22] nanodiamonds,[11,12,23] graphite,[19,24] MWCNT,[11,20,23,25] and other types of porous carbons.[26-28] It is known that some of those materials, e.g. activated carbons, gasify/decompose under the reaction conditions.[23,29-31] On the other hand, MWCNT showed slow catalyst deactivation and good thermal stability under harsh conditions with the deposition of reaction based coke.[32] Schwartz et al. used few layer graphene for the oxidative dehydrogenation of isobutane and identified dicarbonyls at the zigzag edges and quinones at armchair as the active sites.[33] Nanodiamonds also furnished a high selectivity and stability in the ODH of ethylbenzene[11] n-butane[34] and propane.[35] The selectivity is increased by the formation of sp^2 hybridised shell on a sp^3 core (onion-like nanocarbon). Nanodiamonds have typical dimensions smaller than 10 nm. Therefore, for a practical implementation of nanodiamonds as catalyst, their dispersion in three-dimensional macrostructures is highly desired. To this end, effort have been made to support nanodiamonds on CNT/SiC monoliths,[36] on few layer graphene[37] and on GO.[38] The supporting of nanodiamonds on graphene may prevent the restacking of graphene and the agglomeration of nanodiamonds at the same time.

Herein, we have prepared graphene aerogels by reduction and self-assembling of graphene oxide under hydrothermal conditions. Using a single step strategy, nanodiamonds have been dispersed on the surface of graphene aerogel concomitantly with the reduction and self-assembling process. The materials with different nanodiamond content have been characterised by TEM, SEM, Raman spectroscopy, and X-ray photo electron spectroscopy. The catalytic performance of the prepared materials

in the oxidative dehydrogenation of propane has been compared with that of carbon nanotubes.

Experimental

Partially reduced GO aerogel was synthesized by hydrothermal reduction. To this end, 16 ml of a 2 mg/mL of GO aqueous dispersions (Graphenea) was introduced on an teflon-lined autoclave at 195 ºC during 18 hours. To prepare the graphene-nanodiamond hybrids a aliquot of a 5 wt.% nanodiamond aqueous dispersion (Carbodeon) was added to the GO dispersion. The volume of the aliquot was calculated to achieve nominal loading of 2, 5, 10 wt% with respect to the weight of GO. The dispersion of graphene and nanodiamond was introduced in the autoclave and treated at the same conditions as stated above. After 18 hours in the autoclave, a monolithic hydrogel is obtained which takes the shape of the mould in the autoclave. The hydrogel is dried by freeze drying becoming an aerogel which is subsequently stored for characterising and testing in propane dehydrogenation reaction. The prepared materials are denoted as RGO, (standing for reduced graphene oxide), RGO-2%ND, RGO-5%ND, RGO-10%ND. The number before ND stands for weight percentage of nanodiamonds added to the starting GO dispersion.

For characterisation of GO, it was precipitated from GO dispersion with HCl and subsequently dried. Carbon nanotubes (CNT, Baytubes®) were purchased from Bayer MaterialScience AG and treated with 65% HNO_3 under reflux during 18 h to remove any traces of metal and create oxygen functional groups. This catalyst is named as CNT-O.

The catalysts produced were characterized by X-ray photoelectron spectroscopy (XPS). The XPS system used was an ESCAPlus Omnicrom equipped with a Mg Kα radiation

source to excite the sample. Calibration of the instrument was performed with Ag $3d_{5/2}$ line at 368.27eV. All measurements were performed under UHV, better than 10^{-10} Torr. Internal referencing of spectrometer energies was made using the C 1s signal at 284.6 eV. The curve fitting of the XPS spectra was performed using CASA XPS software after applying a Shirley baseline. For peak deconvolution, the FWHM was fixed equal for all the peaks and with a maximum value of 2.5 eV.

Surface areas were determined by N_2 adsorption at 77 K (BET) using a Micromeritics ASAP 2020 apparatus, after outgassing for 4 h at 423 K. From the physisorption measurements with N_2, the specific surface area has been calculated by the BET (Brunauer, Emmet, and Teller) theory in the relative pressure range 0.01–0.10 following standard ASTM-4365, which is applicable to microporous materials. Total pore volume (VT) was calculated from the amount of N_2 adsorbed at a relative pressure of 0.99. In addition, it was also determined by CO_2 adsorption (Dubinin-Radushkevich) at 273 K in the same apparatus, after outgassing under the same conditions.

Raman characterisation was performed in a Horiba Jobin Yvon, LabRAM HR UV-VIS NIR. Raman spectra were recorded with an Ar-ion laser beam at an exciting radiation wavelength of 532 nm. The subtraction of the baseline and the fitting of the peaks was performed with Originpro8.5 software.

X-ray diffraction (XRD) patterns were recorded using a Bruker D8 Advance diffractometer in configuration theta-theta using nickel-filtered CuK α radiation (wave length=1.54 Å), a graphite monochromatic source and scintillation detector. 2Θ angles from 3 to 80 º were scanned with a length step of 0.05 and an accumulation time of 3 s.

Temperature programed desorption (TPD) experiments were conducted in a continuous-flow 6 mm o.d. quartz reactor inside a vertical furnace with a temperature controller (Eurotherm). ~20 mg of catalyst diluted in SiC were placed on quartz wool inside the

reactor. The temperature was controlled with a thermocouple inside the catalytic bed. 50 ml/min of Ar was continuously flow through the catalyst bed. Gas analysis was performed with a Pfeiffer vacuum mass spectrometer. The following m/z signals were recorded in mass spectrometer: 18, 28, 40, 44. When the signals in the spectrometer are stabilised, the temperature is ramped from 273 to 1293 K at 10 ºC/min. The signals of the gases were calibrated taking into account the baseline of Ar and using CO and CO_2 calibrated canisters.

Catalytic testing in oxidative dehydrogenation (ODH) of propane was carried out in a continuous-flow 6 mm o.d. quartz reactor inside vertical furnace with a temperature controller (Eurotherm). 20 mg of catalyst diluted in SiC was placed on quartz wool inside the reactor. The reaction temperature was controlled with a thermocouple inside the catalytic bed. The catalyst was heated under an inert atmosphere until 673 K and stabilised 3 h in Ar and 3h in 5%O_2 in Ar. During this pre-treatment CO and CO_2 were monitored to assess if there is some carbon burn-off. After 2 hours, the CO and CO_2 desorbed were negligible indicating that there is no gasification of catalyst under reaction conditions.

After the stabilisation pre-treatment, ODH reaction was carried out using 20 ml/min of a mixture of propane: oxygen: argon (15:5:80). The reaction was performed until stabilisation of the signal and the values were taken as conversion and selectivities at steady state. The outlet reaction gases were analysed with an Agilent Micro GC 3000A. H_2, O_2, CO and CH_4 were analysed in a molsieve column, CO_2 in a Plot-Q column, and propane and propene in an alumina column. To ensure repeatability, 2–3 separate GC samples were taken and averaged for each experimental data point. After reaction mixture has been introduced, the main products detected (>99%) were propene, CO and CO_2, ethane and methane. The carbon balance ruled out either carbon products

accumulated on the catalyst or gasification of carbon. The stability of the catalyst under reaction conditions was corroborated by stability test during 24 hours, in which the conversion only dropped about 1%.

Results and discussion

Figure 1 displays representative SEM and TEM images of reduced graphene oxide aerogel (RGO). SEM image suggests a random assembling of the RGO domains, leaving pores between them. Large pores in the range of macroporosity (0.5-1 μm) are visible in the SEM images. The RGO aerogel is compressible, which made the measurement of the porosity by Hg porosimetry unfeasible. However, the high porosity is evidenced by the very low density of the aerogel (~30 mg/cm^3).[39] Considering a true density of graphene of 2 g/cm^3,[40] a simple calculation renders a porosity of 98.5% or 33 cm^3/g. Figure 1b shows that the RGO sheets are crumpled suggesting the presence of abundant defects in the lattice. The surface area is 77 m^2g^{-1} and 935 m^2g^{-1} when measured by N_2 physisorption and CO_2 adsorption, respectively. The discrepancy in surface area value depending on the method of measurement indicates the presence of micropores smaller than 0.7 nm. The DFT pore size distribution applied to the CO_2 adsorption isotherm (Figure S1 supplementary material) confirms the presence of pores with average size of 0.6 nm which can be attributed to the space between the graphene layers. The space between stacked layers in natural graphite is 0.335 nm but the crumples, water intercalation, and oxygen functional groups in the layer may force a larger separation. XRD diffractogram analysis of precipitated starting graphene oxide (GO) (Figure S2 in the Supporting Information) showed a (001) peak at 2θ=10º, corresponding to a interlayering spacing of 0.879 nm, which is substantially larger than natural graphite. This was in agreement with literature values, which state that the

interlayering spacing for GO materials ranges from 0.5 to 0.9 nm.[41] This is a consequence of the water intercalation that penetrates into the space between the graphite layers, as well as of the incorporation of oxygen functional groups in the basal plane during harsh oxidation.[42] After hydrothermal process (RGO), the (001) peak disappeared while the (002) peak, typical of graphitic materials, is now visible at 24.5º, corresponding to an interlayer spacing of 0.367 nm, which is still larger than that of CNT-O (0.342 nm) and natural graphite. The broad and shifted (002) diffraction peak of the RGO aerogel suggests poor ordering of the graphene sheets along the stacking direction and consequently good exfoliation of the graphene sheets, which may be facilitated by the creasing of graphene sheets.

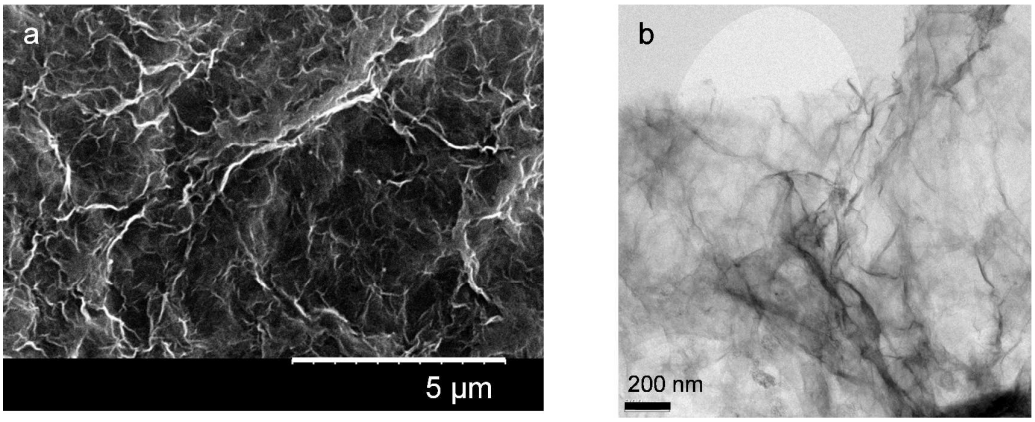

Figure 1. Representative SEM image (a) and TEM image (b) of graphene aerogel

Figure 2 displays representative SEM and TEM images of RGO-2%ND, RGO-5%ND and RGO-10%ND hybrids. No morphological differences were noticed by SEM analysis between RGO+ND hybrid aerogel (Figure 2a) and RGO without nanodiamonds (Figure 1a). TEM images (Figure 2 b-f) clearly showed the presence of small features corresponding to the nanodiamonds, which are homogeneously distributed on the

graphene sheets. It is apparent that the density of nanodiamond domains on RGO increases with its loading. For the highest loadings (5-10% ND), nanodiamond clusters are observed and even some nanodiamonds seems to be placed on top of others (Figure 2 d). XRD diffraction pattern of RGO-ND hybrid material (Figure S2 of Supporting Information) is apparently a superposition of the characteristic features of both RGO and nanodiamond materials, showing the (002) peak characteristic of graphite and (111) diffraction peak dominating the XRD pattern of nanodiamond material. Curiously, when ND are used the (002) diffraction peak shifted to $2\theta = 26^{\circ}$, which is closer to the typical position for graphite, suggesting that the water deintercalation and oxygen groups removal has been more effective in the presence of ND.

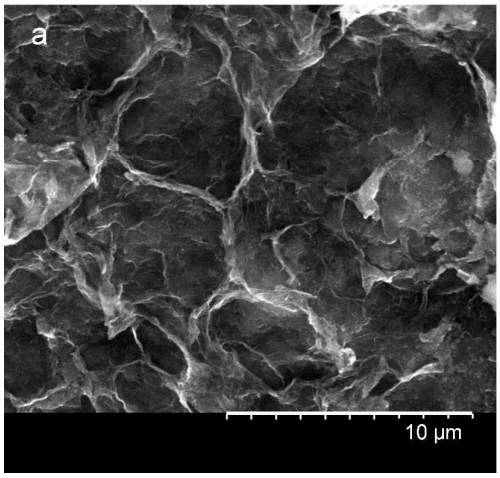

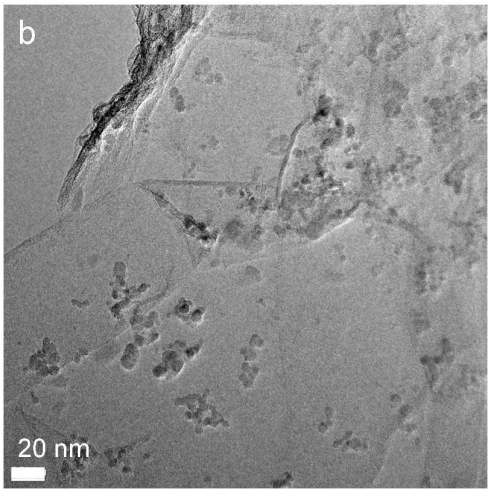

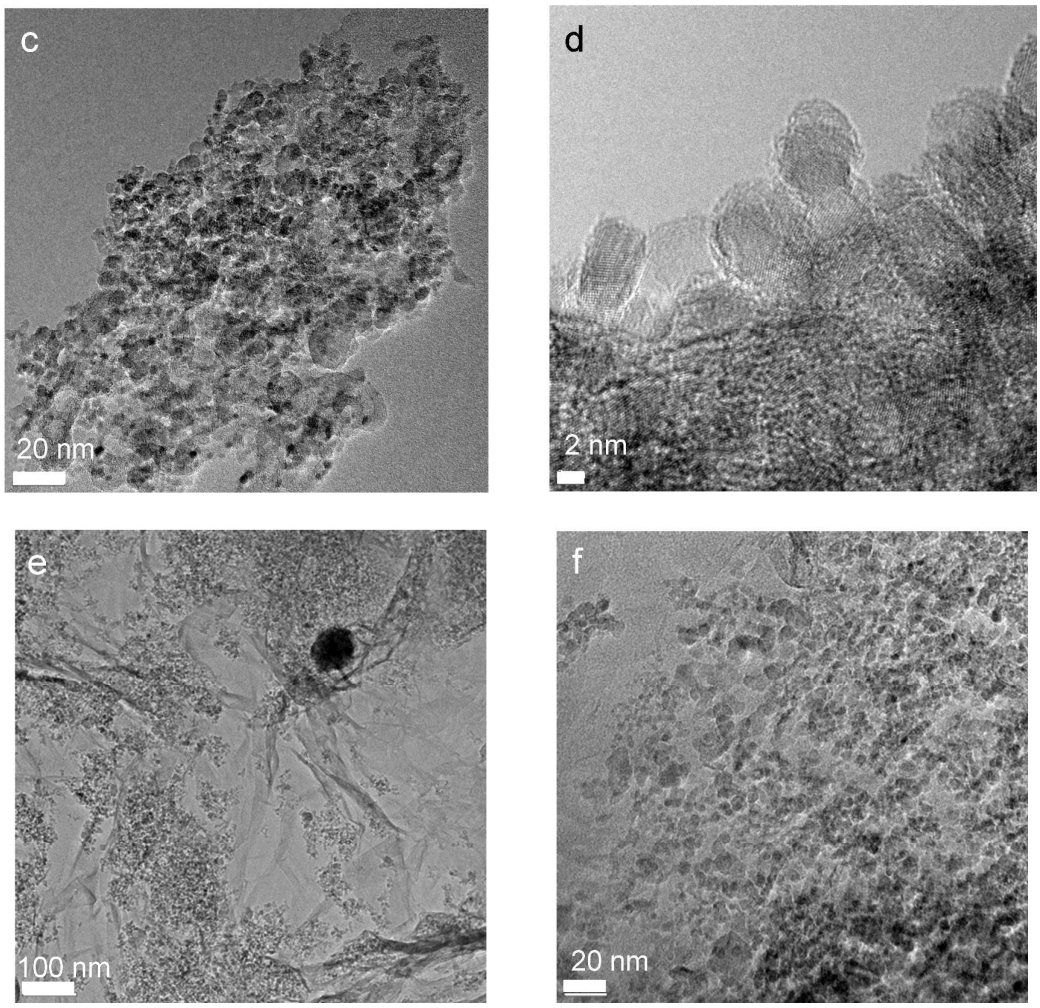

Figure 2. Representative SEM and TEM images of nanodiamonds-graphene hybrids: (a) representative SEM image of RGO-10%ND; (b) representative TEM image of RGO-2%ND; (c) representative TEM image of RGO-5%ND; (d) high-magnification detail of a nanodiamond particle in sample RGO-5%ND; (e,f) Representative TEM images of sample RGO-10%ND at two magnifications.

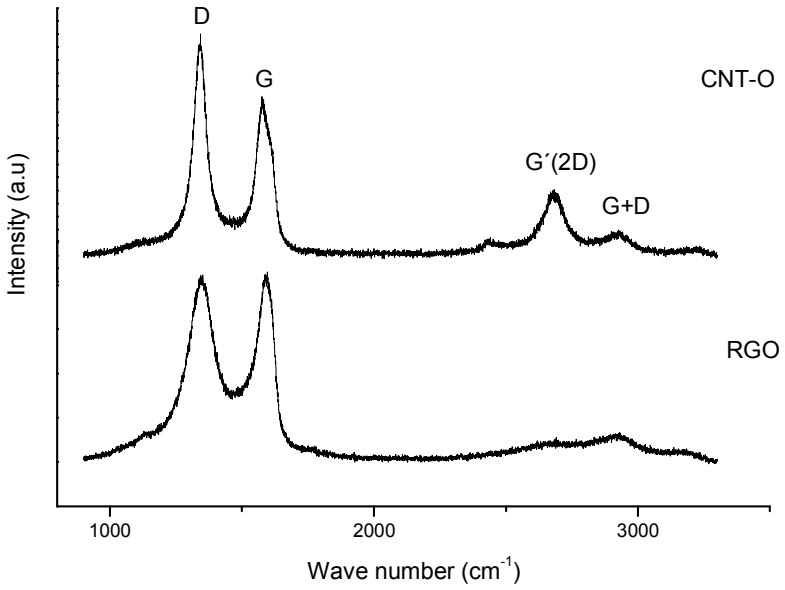

Figure 3. First and second order Raman spectra of CNT-O and RGO

Numerous efforts have been devoted to quantify defects and disorder using Raman spectroscopy for nanographites, amorphous carbons, carbon nanotubes, and graphene. The first attempt was the pioneering work of Tuinstra and Koenig.[43] The Raman spectra of RGO+nanodiamond hybrids were apparently similar to that of RGO (Figure S3 of supplementary information), indicating that the basic structure of RGO is retained in the hybrids. Both CNT-O and RGO spectra (Figure 3) exhibit prominent G (1578-1588 cm^{-1}) and D (~1344 cm^{-1}) bands, which are caused by the active E_{2g} phonon (in-plane optical mode) of sp^2 carbon and the symmetric A_{1g} mode, respectively. Other visible bands are the G′ (or 2D), G+D and 2G bands at ~2685, ~2926, and ~3209 cm^{-1}, respectively.[44] The Raman spectrum of CNT-O displays some significant differences compared to that of RGO. One is that the G′ peak of CNT-O is more intense than that of RGO. The G′ peak of RGO is hardly discernible because only a bump is observed (Figure 3). Similar results have been already reported for graphene with a high disorder

degree, which is typical for materials prepared using the Hummers-Offeman method.[45,46] The G´ band gives a hint about the higher amount of defects in RGO compare to CNT-O. Another difference between CNT-O and RGO spectra is that RGO spectrum exhibits a broad shoulder between D and G bands. In analysis of Raman spectra of many graphitic materials, this shoulder is neglected because is very weak and only D and G bands are considered.[43] Nevertheless, this shoulder is described in the Raman spectra of some carbon materials such as soot,[44] carbon blacks[47] and functionalized graphenes.[48] According to the literature, we have fitted the first-order Raman spectral region (1000–2000 cm^{-1}) of the different materials prepared to five peaks: G (1578-1588 cm^{-1}, attributed to an ideal graphitic lattice with E_{2g} symmetry), D (1340-1347 cm^{-1}, attributed to a disordered graphitic lattice with A_{1g} symmetry), D´ (1606-1612 cm^{-1}, disordered graphitic lattice with E_{2g} symmetry), D´´ (1487-1535 cm^{-1}, amorphous carbon fragments that may include functionalized small molecules),[44,47,49-52] and D* (1100-1167 cm^{-1}, disordered graphitic lattice with A_{1g} symmetry, and ionic impurities).[44,49,53] G, D and D´ have been fitted to Lorentzian functions and D´´ and D* to Gaussian functions since peak D´´ is reported to fit better to a Gaussian curve.[44,47,53] The sum of the five proposed functions shows good agreement with the experimental spectrum. As example of fitting, Figure 4 compares the fitting of CNT-O and RGO first-order Raman region. The rest of fitted spectra are shown in Figure S4 of Supplementary information. It was not possible to record the Raman spectrum of pristine nanodiamond due to the high fluorescence of this sample. The parameters of the fitting (positions and area ratios of peaks) of all samples are listed in Table 1.

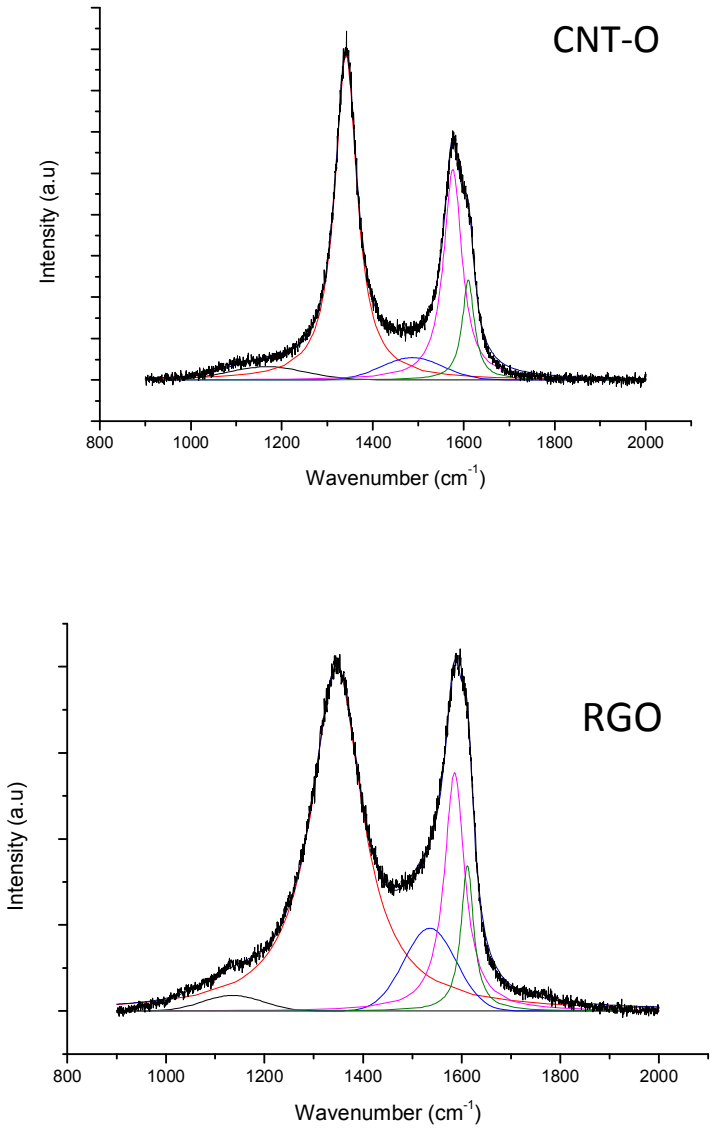

Figure 4. Fitting of first-order Raman spectra of CNT-O and RGO. (—) D peak, (—) G peak, , (—) G´ peak, (—) D´´ peak, (—) D* peak.

Table 1. Parameters of the fitting of Raman spectra.

	Band Positions (cm^{-1})					Band area ratios		
	D*	D	D´´	G	D´	D/G	D´´/G	D*/G
CNT-O	1167	1341	1487	1576	1610	1.9	0.24	0.17
GO	1100	1351	1535	1582	1610	4.2	0.53	0.10
RGO	1135	1346	1535	1585	1611	3.6	0.59	0.13
RGO+2% ND	1124	1347	1528	1587	1612	3.3	0.39	0.13
RGO+5% ND	1129	1344	1525	1584	1609	3.3	0.39	0.10
RGO+10%ND	1101	1340	1521	1582	1606	3.4	0.38	0.20

Comparatively, CNT-O exhibits D/G and D´´/G ratios lower than those of RGO sample. The higher D/G ratio of RGO is attributed to the graphene edges or defects in the disordered graphitic lattice[54] in agreement with the creased structure found in TEM and higher amount of oxygen functional groups. This would logically result in a high surface area material. Note that the D/G ratio varied inversely with the crystallite size, L_a.[43] When NDs are added to RGO, the D/G ratio does not vary appreciably. Thereby, NDs does not introduce more defects on graphene or the defects added by NDs are compensated by healing some defects of RGO. This agrees with the more ordered structure when ND are introduced indicated by the shift of the XRD (002) diffraction peak. This finding contrasts with results of other researchers,[37] in which the D/G intensity ratio increases significantly when NDs are adsorbed although they used less defective few layer graphene from exfoliation of expanded graphite.

The higher D´´/G ratio is usually attributed to higher content of organic fragments, amorphous carbon and functional groups in the sample. The fitting indicates that the D´´/G decreases substantially in the RGO-ND hybrid respect to RGO suggesting that functional groups of the RGO are removed when nanodiamonds are added, in good

agreement with the XRD observations. In addition, a substantial increase of the D*/G ratio occurs for the hybrid with the highest nanodiamond content. The D* band has been related to disordered graphitic lattice of soot provided by the existence of sp^3 bonds.[44,53] Thus, the increase of D*/G ratio may point out to an increase of the number of sp^3 bonds for the hybrid with higher nanodiamond content. The sp^3/sp^2 is also quantified below by XPS.

The Raman of precipitated GO was also recorded (entry 2 in table 1) and its D/G, D´´/G, D*/G ratios are very similar to that of RGO. The D/G ratio decreases slightly upon reduction, in contrast to other reduction methods in which the D/G ratio increases due to a decrease in size of the sp^2 domains.[55] Accordingly, the hydrothermal reduction is a mild method that does not break the graphitic domains of GO into smaller ones.

The surface oxygenated groups have been analyzed by XPS (Figure S6-S8). The O*1s* and C*1s* spectra or selected samples are shown in Figure 5. The following groups of functionalities were considered for fitting of C 1s peak: aromatic and aliphatic carbon (sp^2 C-C, 284.6 eV), carbon in sp^3 hybridization of nanodiamond and to single oxygen in hydroxyl groups or ethers (sp^3 C, 286±0.1 eV), carbonyl and quinone groups (>C=O, 287±0.1 eV), carboxylic groups (O-C=O, 288.3±0.1 eV) and the π- π* interaction (290.6±0.3 eV).[56-59] The C1s core-level spectrum of the CNT (Figure 5) and RGO (Figure S5 of supplementary information) exhibits a dominant peak at 284.6 eV due to carbon atoms of the graphene sheets (C=C, C-H, C-C). However, the spectrum is remarkably different after the formation of the hybrid with nanodiamonds (Figure 5a). The spectrum of hybrid combines contributions of RGO (sp^2, carboxylic groups, π- π* interaction) and of nanodiamond (sp^3 and carbonyl/quinone). Table 2 compiles the parameters of the fitting of XPS C*1s* peak and the calculated sp^3/sp^2 ratio. The lowest

ratio corresponds to CNT-O (0.16) and RGO (0.19) and the highest ratio to ND (7.9). The RGO+ND hybrids furnished sp^3/sp^2 ratios between RGO and ND, increasing as ND content rises.

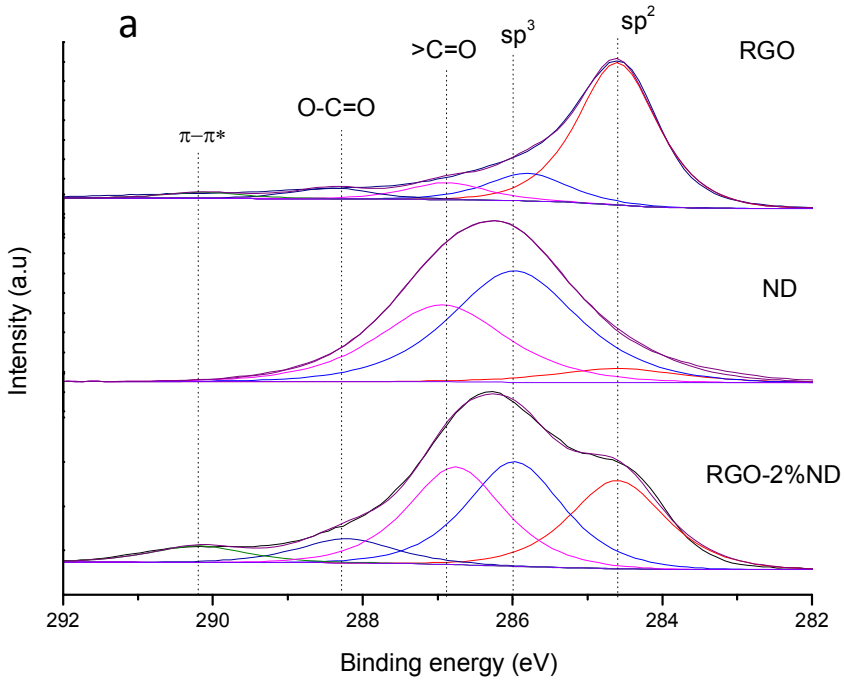

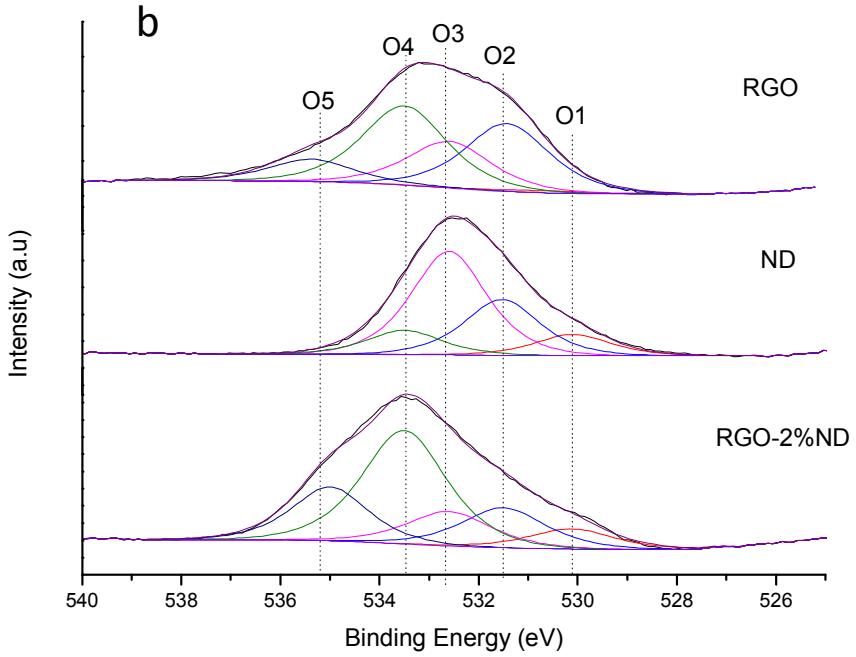

Figure 5. XPS C1*s* (a) and O1*s* (b) core-level spectra of reduced graphene oxide, nanodiamond and their hybrid (RGO-2%ND).

According to our analysis, the XPS O1s spectrum can be divided into the following regions (Figure 5b): O1 (530.1-530.7 eV) corresponds to highly conjugated forms of carbonyl oxygen such as quinone or pyrone groups;[60-62] O2 (531.5±0.1 eV) is assigned to a carbon−oxygen double bond; O3 (532.6±0.1 eV) is a carbon−oxygen ether-like single bond; O4 (533.5±0.1 eV) refers to carbon oxygen single-bonds in hydroxyl groups; and O5 (535.2±0.1 eV) is assigned to chemisorbed water and/or oxygen.[59]

Table 2. Parameters of quantification of XPS 1Cs core level spectra of all samples

	Relative abundance of each peak					sp^3/sp^2
	sp^2 (284.6 eV)	sp^3 (286±0.1 eV)	>C=O (287±0.1 eV)	O-C=O (288.3±0.1 eV)	π- π* (290.6±0.3 eV)	
CNT-O	69.6	10.9	5.1	5.9	8.4	0.16
ND	6.9	55.0	38.0	0	0	7.95
RGO	67.8	12.7	8.6	8.2	2.7	0.19
RGO-2%ND	26.7	31.6	29.5	7.3	4.9	1.18
RGO-5%ND	24.2	30.8	32.1	8.1	4.8	1.27
RGO-10%ND	24.3	32.5	27.7	10.6	4.8	1.33

Compared to CNT-O and RGO (Figure 5b and Table 3), nanodiamond has much higher percentage of O1 (carbonyl in conjugated form) and O3 (ether-like oxyen) and much

lower or negligible O4 (single bonded hydroxyl groups) and O5 (chemisorbed water). The O content follows this order RGO>ND>>CNT-O. One peculiarity of CNT-O is that it lacks the O3 or ether-like oxygen.

Figure 6 compares some XPS parameters of the different carbon materials such as sp^2/sp^3 ratio, total O/C ratio and (O1+O2)/C ratio. O1+O2 encompass carbonyl+quinone groups, which are reported as the active sites for the propane dehydrogenation reaction.[33,63,64]

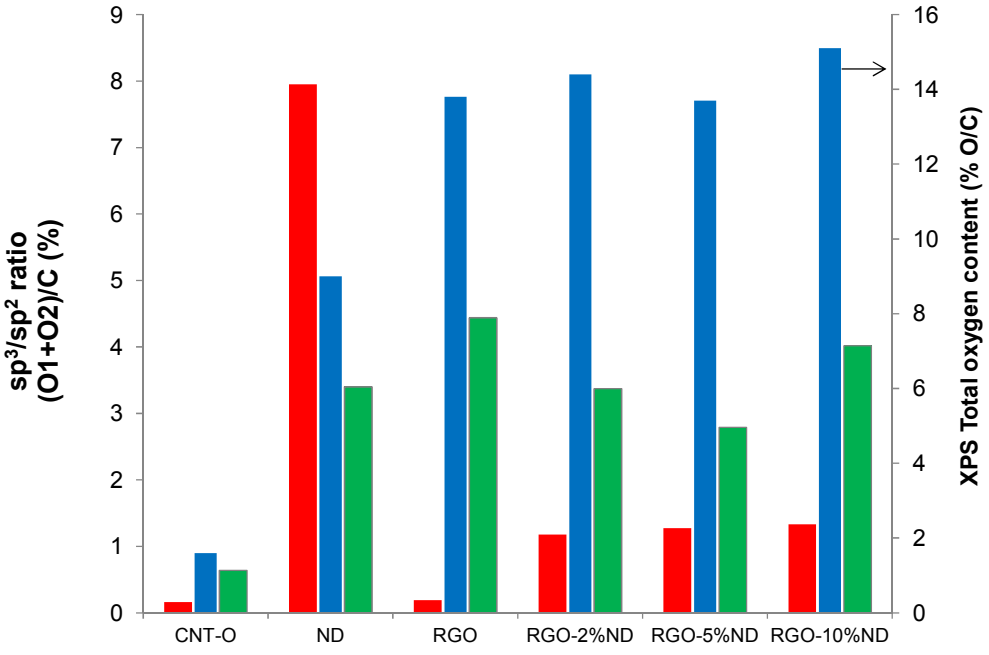

Figure 6. sp^2/sp^3 determined from XPS C 1s peak ( ), total oxygen content ( ) and (O1+O2)/C ratio ( ) from XPS O 1*s*.

Table 3. Parameters of quantification of XPS 1Os core level spectra of all samples

	Relative abundance of each peak (%)					O/C
	O1 (530.4-±0.3 eV)	O2 (531.5±0.1 eV)	O3 (532.6±0.1 eV)	O4 (533.5±0.1 eV)	O5 (535.2±0.1 eV)	at%
CNT-O	0	40.0	0	48.2	11.8	1.6
ND	10.4	27.3	50.5	11.8	0	9.0
RGO	1	31.1	21.4	36.3	10.2	13.8
RGO-2%ND	7.9	15.6	13.4	44.1	18.9	14.4
RGO-5%ND	4.7	15.6	15.9	37.1	26.7	13.7
RGO-10%ND	8.6	8.8	26.4	42.8	13.4	15.1

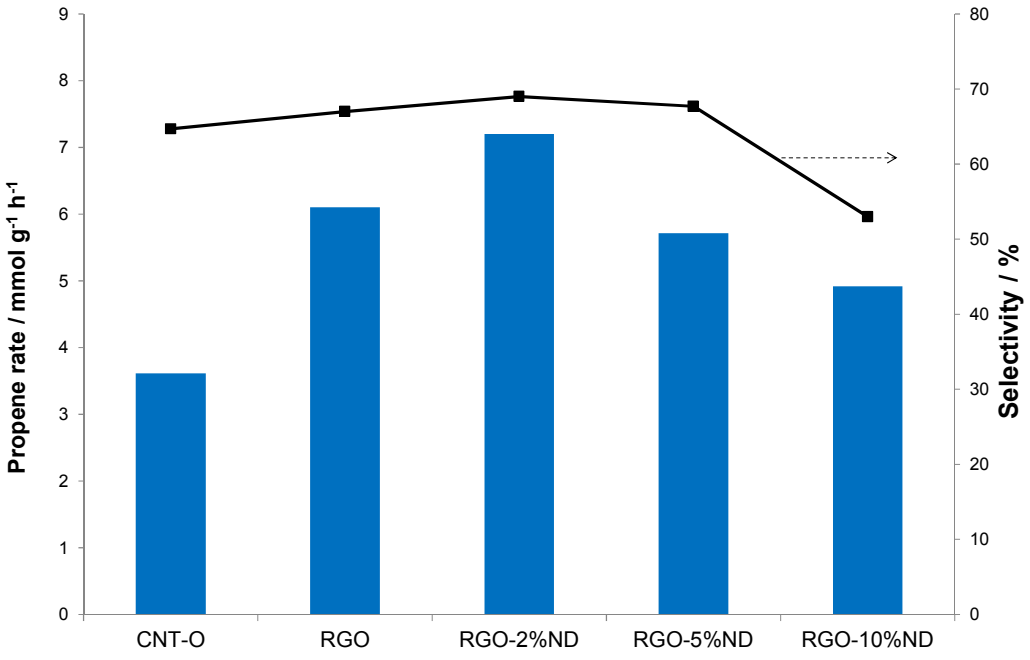

Figure 7. Propene production rate and propene selectivity for propane dehydrogenation at 673 K flowing 20 ml/min of a mixture of propane: oxygen: argon (15:5:80).

The prepared carbon materials were tested in oxidative dehydrogenation (ODH) of propane at 673K. Figure 7 shows the propene productivity and selectivity. RGO provided significantly higher propene production rate than CNT-O. The hybrid RGO-2%ND exhibited 18% larger propene production rate than RGO, while keeping the same selectivity. Further increase of nanodiamond content decreases both propene productivity and selectivity. Similar effect for the nanodiamond content has been recently reported using nanodiamonds on few layer graphene for elthylbenzene dehydrogenation.[65] It was explained by the higher nanodiamond dispersion of the lowest nanodiamond contents. In our RGO-2%ND catalyst, some small nanodiamond aggregates are still observed (Figure 2b), pointing that the dispersion can be still improved, and hence the catalytic performance.

To study the relationship between catalytic performance and surface chemistry, the catalysts after reaction were characterised by temperature programmed desorption (TPD). During TPD, surface oxygen groups on carbon materials decompose upon heating in Ar by releasing CO, CO_2, and H_2O. Figure 8 a and b shows the desorption of CO_2 and CO, respectively, for all the used catalysts. In general, CO desorption is associated to anhydrides (623 to 893 K), phenols (873 to 973 K), or carbonyls/quinones (973 to 1253 K) and CO_2 desorption can be attributed to anhydrides (623 to 893 K) or lactones (823 to 1073 K).[66,67] Carboxylic acid evolution, which occurs at low temperatures, was almost absent in CO_2 profile of these samples because ODH reaction temperature is higher than its decomposition temperature. The assignment of surface oxygen groups through desorption temperatures is not unambiguous because of surface heterogeneity. Differences in the local active site structures such as armchair and zigzag sites or neighbouring surface oxygen complexes can influence the electronic environment of the relevant group.[68] Additionally, the characteristic broadness of

desorption peaks can be an indication of surface heterogeneity and complexity. We did not dare to decompose the CO_2 peak because the presence of only one broad peak in most of the samples and the overlapping temperature range of desorption of anhydrides and lactones rendered the fitting highly ambiguous. Nevertheless, we fitted the CO desorption peak because several shoulders can be discerned (Figure 8b), which are different for the several carbon catalysts. The difference concerns especially to the high temperature peak corresponding to carbonyl/quinones. We are interested in this peak since these particular oxygen groups are generally claimed to be the active sites for oxidative dehydrogenation of alkanes.[33,63,64] The quantitative TPD characterisation results are compiled in table 4. Figure 9 compares the total oxygen content determined by TPD, by XPS and the carbonyl/quinone oxygen groups determined by fitting of TPD CO profile for all used catalysts. In all the used catalysts the O content determined by XPS is slightly larger than that determined by TPD except for CNT-O. This indicates that oxygenated groups on CNT-O are less accessible than those on the RGO-derived catalysts. Most probably some oxygen groups of CNT-O are inside the tubes and thus they are not detected by XPS but are released in TPD as CO or CO_2. Although CNT-O has slightly higher amount of carbonyl/quinone groups determined by TPD than RGO, the later exhibited substantially higher propene productivity than CNT-O. This evidences again that carbonyl/quinone groups in RGO must be more accessible for reaction in agreement with XPS results (Figure 6). Moreover, RGO contains higher amount of defects than CNT-O as demonstrated by Raman (higher D/G and D¨/G ratios), which may also explain the variations in catalytic activity.

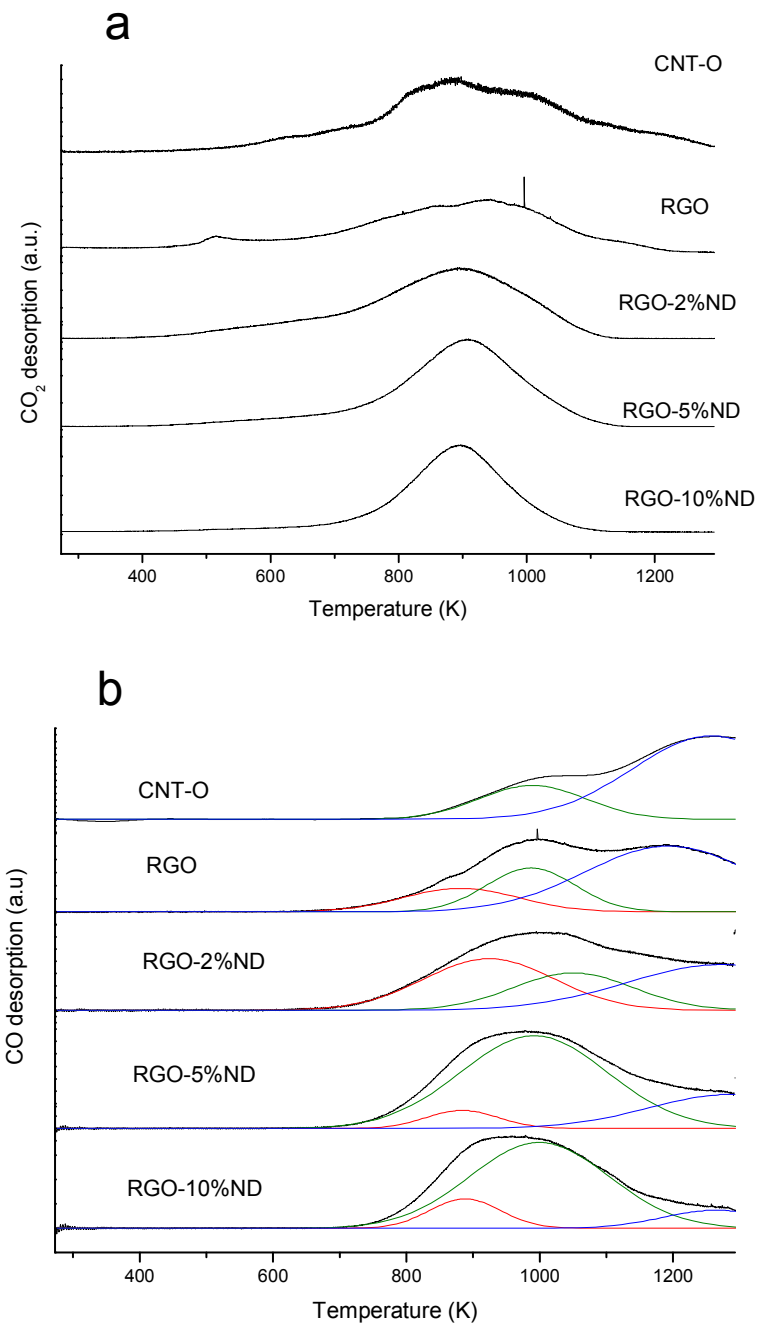

Figure 8. Temperature programmed desorption of CO_2 (a) and CO (b) for the various catalyst after ODH testing.

Table 4. TPD results of quantification and fitting of CO desorption profile

	CO_2	CO	CO desorption fitting Position/K (abundance/%)		
	µmol/g	µmol/g	CO#1	CO#2	CO#3
CNT-O	1621	671	-	989(31)	1257(69)
RGO	1739	967	881(18)	986(25)	1193(57)
RGO-2%ND	2207	969	920(42)	1050(28)	1260(30)
RGO-5%ND	2305	1012	883(7)	991(76)	1287(17)
RGO-10%ND	2869	1372	888 (14)	999(78)	1264(8)

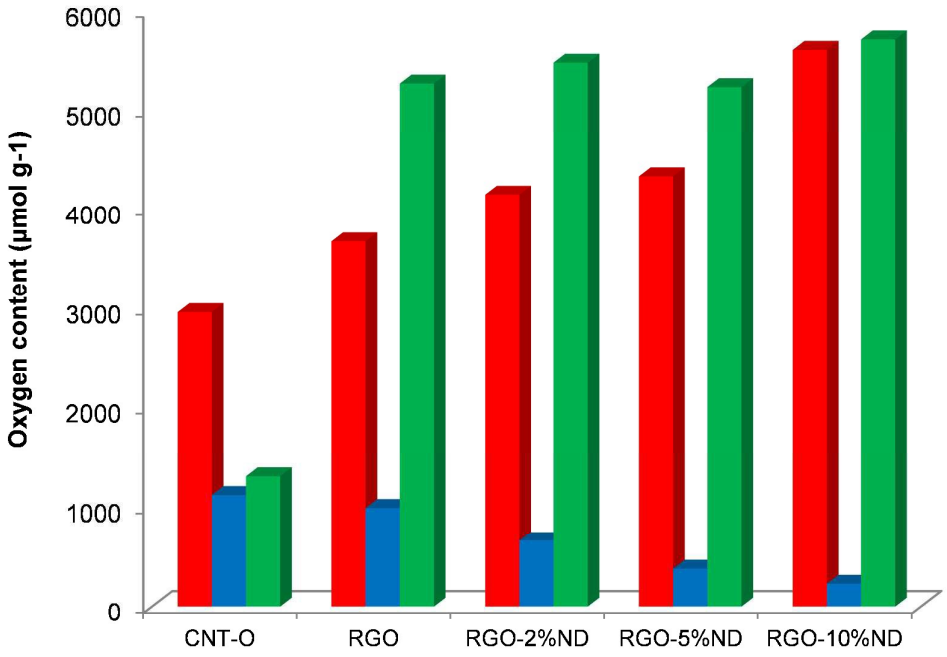

Figure 9. Total oxygen content determined by TPD (■) and XPS (■) and carbonyl/quinone groups determined by TPD (■)

The higher propene production rate for the hybrid RGO-2%ND compared to RGO while keeping the same selectivity could be rationalized because it still contains a high amount of accessible carbonyl-quinone groups and additionally the sp^3/sp^2 character increases substantially (Figure 6). The decrease of propene productivity and selectivity for nanodiamond content higher than 2 wt% could be attributed to the drastic decrease of carbonyl-quinone content (Figure 6 and 9) while total oxygen content increases. From these opposite trends, it can be deduced that the catalysts with increasing nanodiamond loading contain larger amount of other oxygenated groups that are not selective to propene but to total oxidation to CO_2. The decrease of conversion as nanodiamond content rises could be also ascribed to the lower catalytic surface area that is accessible to the reactants for RGO+ND hybrids due to the clustering of nanodiamonds observed by TEM for the highest loadings (Figure 2f). The decrease of D´´/G Raman ratio for the hybrid indicates a decrease of organic fragments or functional groups of RGO which may have also an effect on selectivity and conversion. All these results seem to reconcile previous reports that found that a higher catalytic activity for ODH reaction is associated either with a higher carbonyl-quinone groups content[33,63,64] or with a higher number of accessible edges and defects which are usually quantified by I_D/I_G raman ratio.[69-71]

Conclusions

Reduced graphene oxide aerogels (RGO) have been fabricated by a mild hydrothermal reduction/self-assembly method. This approach renders a highly porous graphene monolith, preserves a significant number of oxygenated groups and defects within graphene sheets and avoids their restacking. In addition, nanodiamonds have been

supported on the surface of RGO aerogels following one-pot strategy. The resulting highly porous aerogel was used as metal-free catalyst in oxidative dehydrogenation of propane for the first time, exhibiting higher propene productivity than oxidised carbon nanotubes (CNT-O) while keeping the same propene selectivity. The outstanding performance of RGO is ascribed to the higher number of defects in the graphitic lattice, higher oxygen content and more accessible carbonyl/quinone groups compared to CNT-O. The formation of the hybrid with low nanodiamond content (2 wt%) provides an 18% increase in the propene productivity, which may be attributed to the increased sp^3/sp^2 ratio. A higher nanodiamond loading afforded lower propene production rate, which is attributed to a drop of carbonyl-quinone group content and to clustering of nanodiamonds. In addition, the selectivity to propene decreased dramatically for the highest nanodiamond content ascribed to an increase of the type of oxygenated groups that are not selective to propene but to total oxidation to CO_2. Among the studied catalyst, reduced graphene aerogel with low nanodiamond content of 2 wt% furnished the best catalytic performance for oxidative dehydrogenation of propane due to the combination of a high content of accessible carbonyl-quinone groups and high sp^3/sp^2 ratio. It is envisaged that increasing nanodiamond loading and dispersion will lead to improved catalytic performance.

Aknowledgements.

The financial support of European Commission (FREECATS project, FP7 Grant agreement nº 280658), from Spanish Ministry MINECO and the European Regional Development Fund (project ENE2013-48816-C5-5-R), and Regional Government of Aragon (DGA-ESF-T66 Grupo Consolidado) are gratefully acknowledged.

Reference List

1. D. R. Dreyer, S. Park, C. W. Bielawski, R. S. Ruoff *Chem. Soc. Rev.* 2010, **39** (1), 228.
2. H. P. Jia, D. R. Dreyer, C. W. Bielawski *Tetrahedron* 2011, **67** (24), 4431.
3. W. Cai, R. D. Piner, F. J. Stadermann, S. Park, M. A. Shaibat, Y. Ishii, D. Yang, A. Velamakanni, S. J. An, M. Stoller, J. An, D. Chen, R. S. Ruoff *Science* 2008, **321** (5897), 1815.
4. W. Gao, L. B. Alemany, L. Ci, P. M. Ajayan *Nat Chem* 2009, **1** (5), 403.
5. C. Gómez-Navarro, J. C. Meyer, R. S. Sundaram, A. Chuvilin, S. Kurasch, M. Burghard, K. Kern, U. Kaiser *Nano Lett.* 2010, **10** (4), 1144.
6. W. S. Hummers, R. E. Offeman *J. Am. Chem. Soc.* 1958, **80** (6), 1339.
7. S. Tang, Z. Cao *Phys. Chem. Chem. Phys.* 2012, **14** (48), 16558.
8. M. M. Bhasin, J. H. McCain, B. V. Vora, T. Imai, P. R. Pujad *Appl. Catal. A: Gen.* 2001, **221** (1–2), 397.
9. B. M. Weckhuysen, R. A. Schoonheydt *Catal. Tod.* 1999, **51** (2), 223.
10. T. G. Alkhazov *Reac. Kin. Catal. Lett.* 1979, **12** (2), 189.
11. J. Zhang, D. S. Su, R. Blume, R. Schlögl, R. Wang, X. Yang, A. Gajovic *Angew. Chem. Int. Ed.* 2010, **49** (46), 8640.
12. N. Keller, N. I. Maksimova, V. V. Roddatis, M. Schur, G. Mestl, Y. V. Butenko, V. L. Kuznetsov, R. Schlögl *Angew. Chem. Int. Ed.* 2002, **41** (11), 1885.
13. D. S. Su, N. Maksimova, J. J. Delgado, N. Keller, G. Mestl, M. J. Ledoux, R. Schlögl *Catalysis Today* 2005, **102–103**, 110.
14. D. Su, N. I. Maksimova, G. Mestl, V. L. Kuznetsov, V. Keller, R. Schlögl, N. Keller *Carbon* 2007, **45** (11), 2145.
15. J. J. Delgado, D. S. Su, G. Rebmann, N. Keller, A. Gajovic, R. Schlögl *J. Catal.* 2006, **244** (1), 126.
16. J. J. Delgado, X. W. Chen, B. Frank, D. S. Su, R. Schlögl *Catal. Tod.* 2012, **186** (1), 93.
17. J. J. Delgado, R. Vieira, G. Rebmann, D. S. Su, N. Keller, M. J. Ledoux, R. Schlögl *Carbon* 2006, **44** (4), 809.

18. P. Li, T. Li, J. H. Zhou, Z. J. Sui, Y. C. Dai, W. K. Yuan, D. Chen *Mic. Mes. Mater.* 2006, **95** (1–3), 1.

19. G. Mestl, N. I. Maksimova, N. Keller, V. V. Roddatis, R. Schlögl *Ang. Chem. Inter. Ed.* 2001, **40** (11), 2066.

20. D. S. Su, X. Chen, X. Liu, J. J. Delgado, R. Schlögl, A. Gajovic *Adv. Mater.* 2008, **20** (19), 3597.

21. T. J. Zhao, W. Z. Sun, X. Y. Gu, M. Rönning, D. Chen, Y. C. Dai, W. K. Yuan, A. Holmen *Appl. Catal. A: Gen.* 2007, **323**, 135.

22. M. F. Pereira, J. J. M. Orfao, J. L. Figueiredo *Carbon* 2002, **40** (13), 2393.

23. J. Zhang, D. Su, A. Zhang, D. Wang, R. Schlögl, C. Hébert *Angew. Chem. Int. Ed.* 2007, **46** (38), 7319.

24. A. Guerrero-Ruiz, I. Rodríguez-Ramos *Carbon* 1994, **32** (1), 23.

25. N. V. Qui, P. Scholz, T. Krech, T. F. Keller, K. Pollok, B. Ondruschka *Catal. Comm.* 2011, **12** (6), 464.

26. Y. Du, J. Li, X. Yang *Catal. Comm.* 2008, **9** (14), 2331.

27. D. S. Su, J. J. Delgado, X. Liu, D. Wang, R. Schlögl, L. Wang, Z. Zhang, Z. Shan, F. S. Xiao *Chem. :Asian J.* 2009, **4** (7), 1108.

28. L. Wang, J. J. Delgado, B. Frank, Z. Zhang, Z. Shan, D. S. Su, F. S. Xiao *ChemSusChem* 2012, **5** (4), 687.

29. M. F. R. Pereira, J. J. M. Orfao, J. L. Figueiredo *Appl. Catal. A: Gen.* 2001, **218** (1–2), 307.

30. M. F. R. Pereira, J. J. M. Orfao, J. L. Figueiredo *Coll. Surf. A: Phys. Eng. Asp.* 2004, **241** (1–3), 165.

31. A. Rinaldi, J. Zhang, J. Mizera, F. Girgsdies, N. Wang, S. B. A. Hamid, R. Schlogl, D. S. Su *Chem. Commun.* 2008, (48), 6528.

32. V. Zarubina, H. Talebi, C. Nederlof, F. Kapteijn, M. Makkee, I. Melián-Cabrera *Carbon* 2014, **77**, 329.

33. G. K. P. Dathar, Y. T. Tsai, K. Gierszal, Y. Xu, C. Liang, A. J. Rondinone, S. H. Overbury, V. Schwartz *ChemSusChem* 2014, **7** (2), 483.

34. X. Liu, B. Frank, W. Zhang, T. P. Cotter, R. Schlögl, D. S. Su *Angew. Chem. Int. Ed.* 2011, **50** (14), 3318.

35. X. Sun, Y. Ding, B. Zhang, R. Huang, D. Chen, D. S. Su *ACS Catal.* 2015, 2436.

36. H. Liu, J. Diao, Q. Wang, S. Gu, T. Chen, C. Miao, W. Yang, D. Su *Chem. Comm.* 2014, **50** (58), 7810.

37. T. T. Thanh, H. Ba, L. Truong-Phuoc, J. M. Nhut, O. Ersen, D. Begin, I. Janowska, D. L. Nguyen, P. Granger, C. Pham-Huu *J. Mater. Chem. A* 2014, **2** (29), 11349.

38. Z. Zhao, Y. Dai, G. Ge, Q. Mao, Z. Rong, G. Wang *ChemCatChem* 2015, **7** (7), 1070.

39. H. P. Cong, J. F. Chen, S. H. Yu *Chem. Soc. Rev.* 2014, **43** (21), 7295.

40. M. Gaboardi, A. Bliersbach, G. Bertoni, M. Aramini, G. Vlahopoulou, D. Pontiroli, P. Mauron, G. Magnani, G. Salviati, A. Zuttel, M. Ricco *J. Mater. Chem. A* 2014, **2** (4), 1039.

41. V. Schwartz, W. Fu, Y. T. Tsai, H. M. Meyer, A. J. Rondinone, J. Chen, Z. Wu, S. H. Overbury, C. Liang *ChemSusChem* 2013, **6** (5), 840.

42. J. Che, L. Shen, Y. Xiao *J. Mater. Chem.* 2010, **20** (9), 1722.

43. F. Tuinstra, J. L. Koenig *J. Chem. Phys* 1970, **53** (3), 1126-&.

44. A. Sadezky, H. Muckenhuber, H. Grothe, R. Niessner, U. Pöschl *Carbon* 2005, **43** (8), 1731.

45. E. H. Martins Ferreira, M. V. O. Moutinho, F. Stavale, M. M. Lucchese, R. B. Capaz, C. A. Achete, A. Jorio *Phys. Rev. B* 2010, **82** (12), 125429.

46. A. C. Ferrari *Phys. rev. lett.* 2006, **97** (18), 187401.

47. T. Jawhari, A. Roid, J. Casado *Carbon* 1995, **33** (11), 1561.

48. A. Cuesta, P. Dhamelincourt, J. Laureyns, A. Martínez-Alonso, J. M. D. Tascón *Carbon* 1994, **32** (8), 1523.

49. P. A. Goodman, H. Li, Y. Gao, Y. F. Lu, J. D. Stenger-Smith, J. Redepenning *Carbon* 2013, **55** (0), 291.

50. R. J. Nemanich *Phys. rev. B, Cond. Mat.* 1979, **20** (2), 392.

51. R. Saito, M. Hofmann, G. Dresselhaus, A. Jorio, M. S. Dresselhaus *Adv. Phys.* 2011, **60** (3), 413.

52. S. Vollebregt, R. Ishihara, F. D. Tichelaar, Y. Hou, C. I. M. Beenakker *Carbon* 2012, **50** (10), 3542.

53. S. Claramunt, A. Varea, D. López-Díaz, M. M. Velázquez, A. Cornet, A. Cirera *J. Phys. Chem. C* 2015, **119** (18), 10123.

54. H. Tao, J. Moser, F. Alzina, Q. Wang, C. M. Sotomayor-Torres *J. Phys. Chem. C* 2011, **115** (37), 18257.

55. S. Stankovich, D. A. Dikin, R. D. Piner, K. A. Kohlhaas, A. Kleinhammes, Y. Jia, Y. Wu, S. T. Nguyen, R. S. Ruoff *Carbon* 2007, **45** (7), 1558.

56. L. Adams, A. Oki, T. Grady, H. McWhinney, Z. Luo *Physica E: Low-dim. Syst. Nan.* 2009, **41** (4), 723.

57. T. I. T. Okpalugo, P. Papakonstantinou, H. Murphy, J. McLaughlin, N. M. D. Brown *Carbon* 2005, **43** (1), 153.

58. W. Xia, Y. Wang, R. Bergstraber, S. Kundu, M. Muhler *Appl. Surf. Sci.* 2007, **254** (1), 247.

59. U. Zielke, K. J. Hüttinger, W. P. Hoffman *Carbon* 1996, **34** (8), 983.

60. Y. Lin, D. Su *ACS Nano* 2014, **8** (8), 7823.

61. R. Arrigo, M. Hävecker, S. Wrabetz, R. Blume, M. Lerch, J. McGregor, E. P. J. Parrott, J. A. Zeitler, L. F. Gladden, A. Knop-Gericke, R. Schlögl, D. S. Su *J. Am. Chem. Soc.* 2010, **132** (28), 9616.

62. J. Lahaye, G. Nanse, P. Fioux, A. Bagreev, A. Broshnik, V. Strelko *Appl. Surf. Sci.* 1999, **147** (1–4), 153.

63. I. Pelech, O. S. G. P. Soares, M. F. R. Pereira, J. L. Figueiredo *Catalysis Today* 2015, **249**, 176.

64. A. Zheng, Y. Chu, S. Li, D. Su, F. Deng *Carbon* 2014, **77**, 122.

65. J. Diao, H. Liu, Z. Feng, Y. Zhang, T. Chen, C. Miao, W. Yang, D. S. Su *Catal. Sci. Tech.* 2015, **5** (11), 4950.

66. J. L. Figueiredo, M. F. R. Pereira, M. M. A. Freitas, J. J. M. Orfao *Carbon* 1999, **37** (9), 1379.

67. J. L. Figueiredo, M. F. R. Pereira, M. M. A. Freitas, J. J. M. Orfao *Ind. & Eng. Chem. Res.* 2007, **46** (12), 4110.

68. A. Montoya 2001.

69. F. Atamny, J. Blöcker, A. Dübotzky, H. Kurt, O. Timpe, G. Loose, W. Mahdi, R. Schlögl *Mol. Phys.* 1992, **76** (4), 851.

70. C. Liang, H. Xie, V. Schwartz, J. Howe, S. Dai, S. H. Overbury *J. Am. Chem. Soc.* 2009, **131** (22), 7735.

71. J. Zhang, X. Liu, R. Blume, A. Zhang, R. Schlögl, D. S. Su *Science* 2008, **322** (5898), 73.

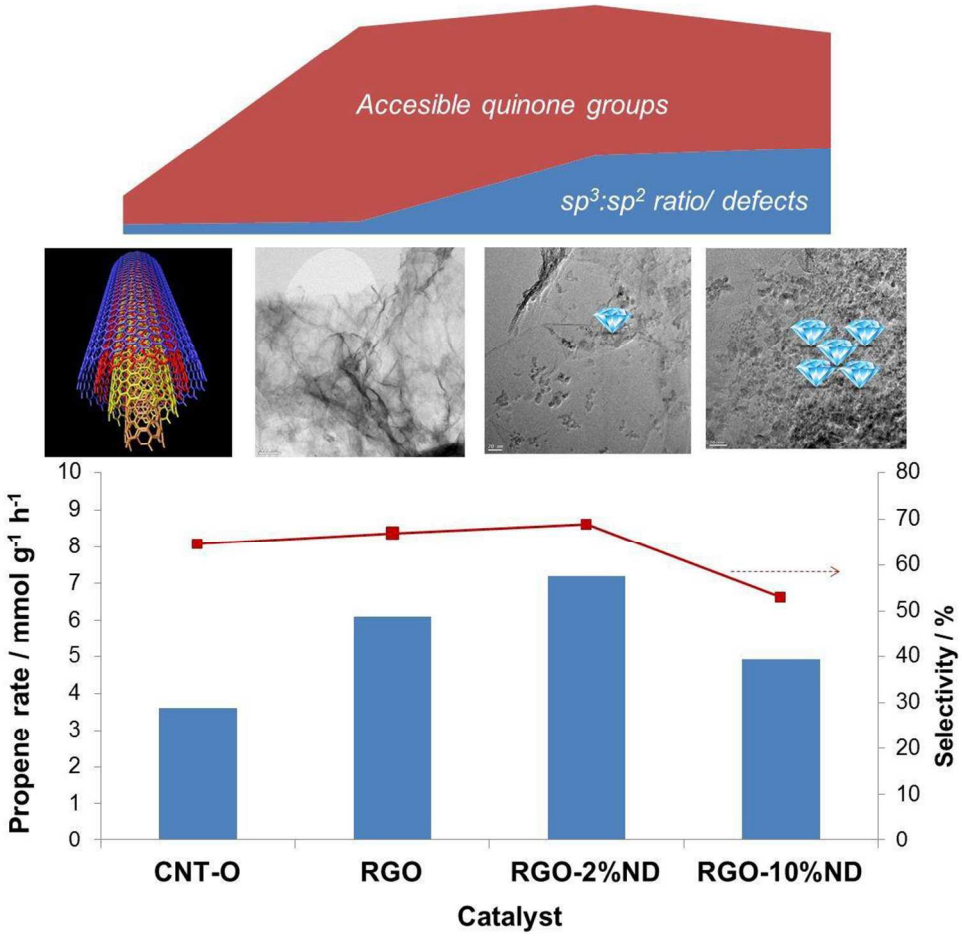

257x252mm (120 x 120 DPI)